Density functional study of amorphous, liquid and crystalline $Ge_2Sb_2Te_5$: homopolar bonds and/or AB alternation?

2008 J. Phys.: Condens. Matter 20 465103

(http://iopscience.iop.org/0953-8984/20/46/465103)

J. Phys.: Condens. Matter **20** (2008) 465103 (10pp) doi:10.1088/0953-8984/20/46/465103

Density functional study of amorphous, liquid and crystalline $Ge_2Sb_2Te_5$: homopolar bonds and/or AB alternation?

J Akola[1,2] **and R O Jones**[1]

[1] Institut für Festkörperforschung, Forschungszentrum Jülich, D-52425 Jülich, Germany
[2] Nanoscience Center, Department of Physics, University of Jyväskylä, PO Box 35, FI-40014, Finland

E-mail: r.jones@fz-juelich.de

Received 10 June 2008, in final form 6 August 2008
Published 30 September 2008
Online at stacks.iop.org/JPhysCM/20/465103

Abstract

The amorphous, liquid and crystalline phases of the phase change material $Ge_2Sb_2Te_5$ (GST) have been studied by means of density functional/molecular dynamics simulations. The large sample (460 atoms and 52 vacancies in the unit cell) and long simulations (hundreds of picoseconds) provide much new information. Here we extend our original analysis (2007 *Phys. Rev.* B **76** 235201) in important ways: partial coordination numbers and radial distribution functions, bond angle distributions, new local order parameters, vibration frequencies, and the charges on atoms and vacancies. The valence band densities of states in amorphous and crystalline GST are compared with ones from x-ray photoemission spectroscopy. The results for the liquid phase are new and those for the crystalline phase much expanded. GST shows pronounced AB alternation (A: Ge, Sb; B: Te), especially in its amorphous phase, and ABAB squares play a central role in the amorphous to crystalline transition. We comment on earlier speculations concerning the nature of the amorphous to crystalline transition.

(Some figures in this article are in colour only in the electronic version)

1. Introduction

The rapid and reversible transition between crystalline and amorphous forms is the basis of phase change (PC) memory materials such as rewritable optical disks. In thin polycrystalline films of these materials, an amorphous nanosized 'bit' can be formed by localized and short (∼1 ns) laser heating to a temperature T above the melting point T_m. The reverse transition to a metastable 'crystalline' form follows longer laser heating (∼50 ns) to below T_m but above the glass transition temperature T_g.[3] The phase change can be monitored by the accompanying large changes in resistivity or optical reflectivity. PC materials are widely viewed as prime candidates for the memory materials of the future, which ideally will be fast (∼10 ns), dense (bit diameter $\ll$50 nm), stable (several years per lost bit), long-lived ($>10^{12}$ cycles per lost bit), and—naturally—with low manufacturing cost and power consumption.

To satisfy these criteria, PC optical memory materials require: (a) an absorption edge in the visible or near infrared that changes with the transition, (b) a melting point T_m that is high enough to prevent spontaneous crystallization, but accessible to laser heating, (c) a rapid and stable transition. Work has focused on semiconductors and semimetals with T_m between 500 and 1000 °C, large atomic mobilities, and structures that are spatially similar in amorphous and crystalline phases. For over 20 years [1, 2], the pseudobinary compounds GeTe–Sb_2Te_3 have attracted much attention, and one of them ($Ge_2Sb_2Te_5$, GST) is already the basis of digital versatile disc-random access memories (DVD-RAM). Another is used in the blu-ray disk (BD), the successor to DVD as optical storage.

Essential to the understanding of the properties of GST is a knowledge of the structures of the different phases, but this is difficult to obtain in a ternary alloy with many vacancies [2–4].

[3] We use the term 'crystal' in the sense of the International Union of Crystallography, i.e. any solid that gives a discrete x-ray diffraction pattern. *Order* is then necessary, not *translational invariance*.

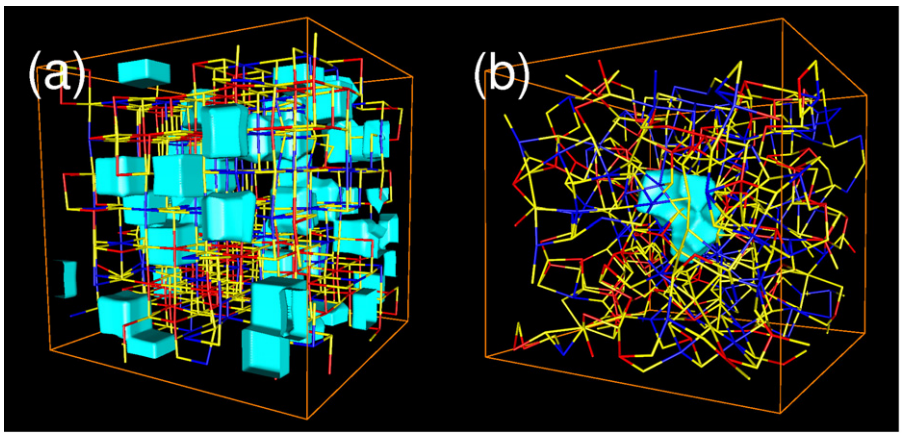

Figure 1. The simulated system of 460 atoms and 52 vacancies in (a) c-GST and (b) a-GST. Red: Ge, blue: Sb, yellow: Te. Vacancies (cavities) are shown as light-blue isosurfaces. A single large cavity (multivacancy) is one of numerous cavities in a-GST.

Yamada [2] proposed that metastable crystalline GST has a rock salt (NaCl, $Fm\bar{3}m$) structure with Te atoms on all Cl:4(a) sites and the Na:4(b) site randomly occupied by Ge and Sb atoms and vacancies. Diffraction methods provide much less information about the amorphous state than about crystalline structures, and calculations present more problems, but there has been progress recently in both areas. High-energy x-ray measurements of the structure factors $S(Q)$ of amorphous and crystalline GST and GeTe [5], for example, were analysed using reverse Monte Carlo (RMC) methods. The partial pair distribution functions so determined suggested that the key to rapid crystallization is the presence of even-numbered rings in crystalline and amorphous GST. If the number and type of bonds are conserved during a phase change, the ring distribution provides a measure of the topological entropy. Bond interchange algorithms can then provide the basis for models of the phase change [6]. On the basis of density functional studies, Lang *et al* [7] proposed that the structure of a-GST is an array of misaligned and distorted eight-membered rings (two Ge, two Sb, four Te). RMC refinement of such a model structure was found to reproduce electron diffraction measurements on thin a-GST films.

Density functional (DF) calculations are free of adjustable parameters, and their combination with molecular dynamics (MD) is ideal to study the structure of amorphous materials. However, the computing resources required for a ternary alloy with many vacancies have restricted earlier DF studies to unit cells with fewer than 100 atoms and timescales of several picoseconds. Essential features of the phase transition are its order–disorder nature and its nanosecond timescale. Small simulation samples cannot exhibit long-range order, and simulation times should be physically relevant, in particular if vibrational and thermodynamic quantities are of interest. We performed recently DF calculations on GST over several hundred nanoseconds in a unit cell containing 460 atoms and 52 vacancies, starting at 3000 K to avoid bias towards particular structural types [8]. A shorter simulation with 270 atoms was carried out by Caravati *et al* [9], and a similar strategy for a much smaller sample (63 and 72 atoms in the unit cell) was carried out subsequently by Hegedüs and Elliott [10].

Our previous work on GST [8] is extended here to provide additional insight into the phase change mechanism. The additional analyses include partial radial distribution functions (RDF), bond angle distributions and local order parameters, and we calculate the charges on the constituent atoms and cavities of amorphous (a-GST, 300 K), liquid (l-GST, 900 K) and metastable crystalline (c-GST, 300 K) phases. We provide the first calculations of the vibration frequencies in a- and c-GST. The simulation method is outlined in section 2, and we present the new results in section 3 and our conclusions in section 4. The earlier literature is surveyed in [8], where more details of the methods of analysis are provided.

2. Methods

DF calculations have been performed with the Car–Parrinello MD package (CPMD) [11], and a full description is provided in [8]. The following details are essential. The starting geometry (figure 1(a)) was a crystalline (NaCl) cell of 512 atomic sites, with the Na sites occupied randomly by Ge/Sb atoms (20% each) and vacancies (10%), and the Cl sites by Te atoms (50%). The sample contains 460 atoms and 52 vacancies; Ge and Sb are represented by 102 atoms each, Te by 256 atoms. The simulations were performed in cubic simulation boxes at the densities of the crystalline (0.033 07 atoms Å^{-3}, box size 24.05 Å) and amorphous (0.030 82 atoms Å^{-3}, 24.62 Å) phases.

The use of Born–Oppenheimer MD (optimization of the electron density for each ionic configuration) has enabled us to use long time steps (250 and 125 au (6.050 and 3.025 fs) for initialization and data collection, respectively). The simulations were started at 3000 K, followed by cooling (42 ps) to the melting point (900 K) and data collection for 21 ps. Further cooling to 300 K over 139 ps was followed by data collection (also for 21 ps) at 300 K. Finally, the system was quenched to 100 K over 74 ps and the resulting structure optimized using Car-Parrinello MD and simulated annealing.

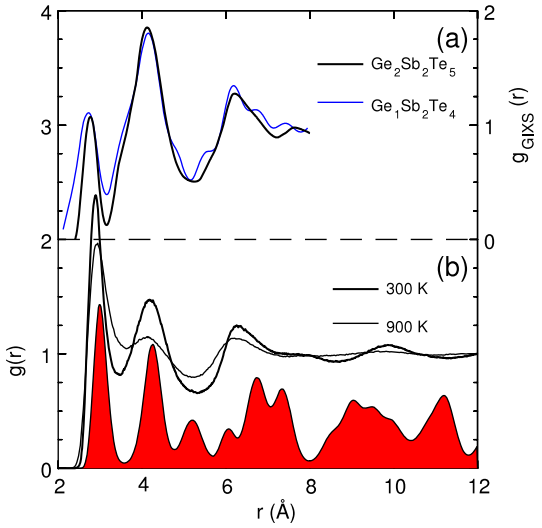

Figure 2. (a) g_{GIXS}: experimental RDF of amorphous $Ge_1Sb_2Te_4$ (black/thick) and $Ge_2Sb_2Te_5$ (blue/thin, GIXS measurement [12] (see footnote 4)). (b) $g(r)$: total RDF of a-GST (thick line) and l-GST (thin line). The filled red area (with a different scale) is for c-GST at 300 K.

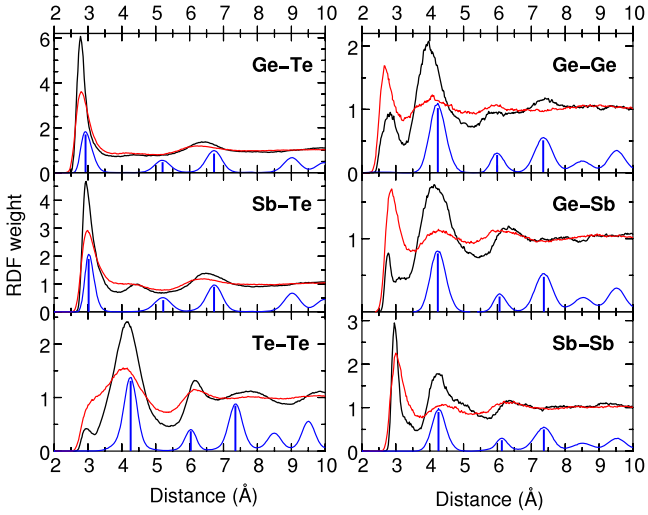

Figure 3. Partial RDF of a- (thick black) and l-GST (red/grey). The blue curve and bars are for c-GST at 300 K (with a different scale).

3. Results

3.1. Radial distribution functions (RDF) and coordination numbers

The positions and velocities of all particles are monitored throughout the simulations, and the RDF can be determined directly. Fourier transformation yields the structure factor $S(Q)$, which can be determined by scattering experiments. Calculated and measured $S(Q)$ are compared in [8]. The calculated total RDF for a-GST (300 K), l-GST (900 K), and c-GST (300 K) (figure 2(b)) shows medium-to long-ranged order in a-GST up to 10 Å, with peaks at 2.88, 4.17, and 6.25 Å and minima at 3.5 and 5.3 Å. These agree well with the corresponding maxima in the RDF determined from grazing incidence x-ray scattering (GIXS) measurements of amorphous thin films of GST alloys (2.8, 4.2, and 6.2 Å) [12][4] (figure 2(a)) and with those determined from x-ray scattering data [5]. Our first peak shows a slight over-estimate of covalent bond lengths. The weaker features in the total RDF at 900 K indicate much reduced order, with no structure after the third maximum (>7 Å). The first peak shifts slightly to 2.92 Å, and the second minimum remains at 5.2 Å. The first three peaks of the total RDF in the amorphous and crystalline phases are very similar, although the former favours shorter bonds (the first two peaks shift from 3.01 Å and 4.26 Å, respectively).

Table 1. Average coordination numbers (cut-off distance 3.2 Å) and binary mixture order parameters of a-GST at 300 K (and l-GST at 900 K).

	N_{tot}	N_{Ge}	N_{Sb}	N_{Te}	α_x
Ge:	4.2 (4.3)	0.4 (0.6)	0.2 (0.6)	3.6 (3.1)	0.77 (0.55)
Sb:	3.7 (3.4)	0.2 (0.6)	0.6 (0.6)	2.9 (2.3)	0.61 (0.37)
Te:	2.9 (2.8)	1.4 (1.2)	1.2 (0.9)	0.3 (0.7)	0.75 (0.40)

Table 2. First maxima and minima of the partial RDF of a-GST at 300 K.

	$R_{\mathrm{max}}/R_{\mathrm{min}}$ (Ge)	$R_{\mathrm{max}}/R_{\mathrm{min}}$ (Sb)	$R_{\mathrm{max}}/R_{\mathrm{min}}$ (Te)
Ge:	2.84/3.22	2.79/2.99	2.78/3.84
Sb:	2.79/2.99	2.96/3.60	2.93/3.88
Te:	2.78/3.84	2.93/3.88	2.95/3.19

The partial RDF at 300, 900 K and for the crystal are shown in figure 3. The coordination numbers, evaluated using a cut-off distance of 3.2 Å, are given in table 1, and the first maxima/minima of the partial RDF are given in table 2. The preference for Ge–Te and Sb–Te bonds in a-GST leads to pronounced peaks at 2.78 and 2.93 Å with coordination numbers of 3.6 and 2.9, respectively. The location of the Ge–Te peak differs from that found from EXAFS measurements (2.61–2.63 Å), where they were assigned to 'tetrahedral Ge atoms' [13, 14]. The range of Ge–Te bonds (lower bound 2.5 Å) does not exclude such bonds, and the slight over-estimate of covalent bond lengths is common in calculations using the PBE functional. The broad Ge–Te and Sb–Te maxima (with first shallow minima at 3.8–3.9 Å) mean that the calculated coordination numbers are sensitive to the choice of cut-off R_{c}. The remaining feature of the Ge–Te RDF is the broad maximum at 6.4 Å, whereas Sb shows a peak at 4.4 Å that matches the second nearest-neighbour distance. Ge and Sb are qualitatively different, since Sb interchanges with Te more readily than does Ge. The first minimum and the second maximum of the Sb–Te RDF disappear on melting.

The presence of Sb atoms and vacancies in the metastable NaCl structure allows Ge–Te bonds to relax, leading to bond lengths between 2.69–3.39 Å and a shorter maximum at 2.92 Å (optimized geometry). The peak has the same maximum at 300 K but is broader, with Ge–Te bonds between 2.6 and 3.5 Å (see figure 3). Sb matches the crystal better, with a Sb–Te bond peak at 3.02 Å and bonds between 2.78–3.46 Å (optimized) and 2.7–3.6 Å (300 K).

[4] The authors note that the amplitudes of the RDF are somewhat uncertain, because the background intensity at low Q has poor quality.

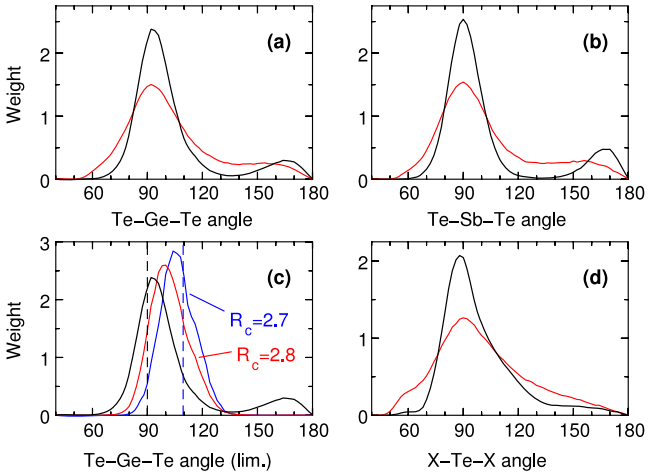

Figure 4. Angular distributions of a-GST (thick black curve) and l-GST (red/grey curve) around (a) Ge, (b) Sb, and (d) Te atoms. The limited angular distributions of a-GST in panel (c) refers to shorter cut-off distances 2.7 (blue) and 2.8 (red) Å. Vertical dashed lines mark octahedral and tetrahedral values.

The Te–Te RDF of the amorphous phase at 300 K shows striking long-range order of Te atoms up to 10 Å, with peaks at 4.16 and 6.14 Å, a minimum at 5.4 Å, and additional maxima at 7.8 and 9.8 Å. The weak maximum at 2.95 Å and the low coordination number (0.3, see table 1) show that there are few Te–Te bonds. There is no long-range order at 900 K, and the first and second peaks merge as the number of Te–Te contacts increases. The Te–Te RDF also shows that Te atoms in a-GST prefer coordination with Ge/Sb, with Te forming the second-neighbour shell. Thermal fluctuations in c-GST lead to peak broadening. For the second maximum in the Te–Te RDF (at 4.26 Å), for example, this is more than 1.5 Å (300 K). There are few Te–Te bonds in c-GST which arise from local distortions around the vacancies.

Figure 3 also shows the partial RDF for the 'homopolar' Ge–Ge, Ge–Sb, and Sb–Sb bonds in a-, l- and c-GST. Common to all pairs is the absence of the nearest-neighbour peak in the rock salt structure ('wrong bonds' [15]), whereas such bonds are present in the amorphous material. These bonds have small weight, and the average coordination numbers are between 0.2 and 0.6 (table 1). As in Te, there is a pronounced second nearest-neighbour peak in curves, but the Sb–Sb RDF has a sharp first peak at 2.96 Å, and Sb is more likely than Te or Ge to form homopolar bonds. Another difference is the maximum at 7.4 Å in the Ge–Ge RDF, close to the third maximum in c-GST. Heating to 900 K results in significant changes in the Ge–Ge and Ge–Sb curves: the first peak now dominates, and the order between 4 and 7 Å moves to shorter range. The Sb–Sb RDF depends less on temperature, and the average coordination numbers at 900 K are 0.6 in each case.

All coordination numbers for a-GST (Ge: 4.2, Sb: 3.7, Te: 2.9) are lower than in the crystalline phase, but larger than the atomic valences (4, 3, 2) suggested by the '$8 - N$ rule', where N is the number of valence electrons. The cut-off is relatively short for Ge–Te and Sb–Te bonds, and inclusion of distances between 3.2 and 4.0 Å results in near sixfold coordination for Ge and Sb. The coordination numbers show that the l-GST (900 K) is less ordered than a-GST. The increase in the total coordination number of Ge at 900 K reflects the larger number of Ge–Ge and Ge–Sb bonds, while Sb and Te become less coordinated.

3.2. Angular distribution functions

The angular distributions of the Te–Ge–Te, Te–Sb–Te, and X–Te–X (X = Ge/Sb) configurations in a- and l-GST are shown in figure 4. Configurations are included if the bonds are shorter than (a) 3.2 Å (figures 4(a), (b), (d)) or (b) 2.7/2.8 Å (figure 4(c)). The distributions around Ge and Sb show octahedral features (a pronounced maximum at 90° and a weaker peak at 180°), and Sb is more strongly peaked than Ge. There is little weight below 60° and above 120° at 300 K, but more at 900 K. The shift in the maximum of Ge in figure 4(a) indicates tetrahedral bonding, and the displacement caused by the restriction to shorter Ge–Te bonds (figure 4(c)) shows that tetrahedral configurations (109.47°) are now more prevalent than octahedra. Sb does not favour tetrahedral coordination under any circumstances. There are very few linear configurations for the short Ge–Te and Sb–Te bonds.

The angular distributions around Te atoms also have a pronounced maximum around 90° (X–Te–X, figure 4(d)), but the reduced weight at 180° differs from Ge and Sb. The range of angles is larger and increases at 900 K, where triangular configurations with bonds between X atoms (Ge/Sb) around 60° are significant. Furthermore, the dihedral angles around Ge–Te and Sb–Te bonds (not shown) display a marked tendency for octahedral (cubic) configurations: maxima at 0°, 90°, and 180°, and minima at 30°, 60°, 120°, and 150° (typical gauche conformations). Cubic arrangements are characteristic of a-GST, since there is little structure in the dihedral angle distribution of the liquid.

3.3. Local order parameters

The topology of nearest neighbours can be discussed conveniently by separating the atoms into types A (Ge, Sb) and B (Te). The local order can be quantified by using order parameters α_x (x = Ge, Sb, Te, table 1) based on the theory of binary liquids [16]:

$$\alpha_x = \frac{1 - n_{AB}/[c_A c_B(n_A + n_B)]}{1 - n_x/[c_A c_B(n_A + n_B)]}, \qquad (1)$$

where c_A and c_B are the concentrations of the atom types A and B, n_A and n_B are the total coordination numbers, and n_{AB} is the AB coordination number. Perfect order (AB alternation) corresponds to $\alpha_x = 1$, a random mixture to $\alpha_x = 0$, and complete phase separation to $\alpha_x = -1$. The calculated order parameters in table 1 show that a-GST is 'semiordered' (values above 0.6), i.e. the structure shows alternating atomic types but has lower coordination than c-GST ($\alpha = 1$). Sb is the least ordered of the three elements. The disorder increases in l-GST, but AB alternation is still significant, particularly in Ge.

All type A atoms (Ge/Sb) in c-GST are coordinated octahedrally to Te atoms (type B), and this suggests a new order

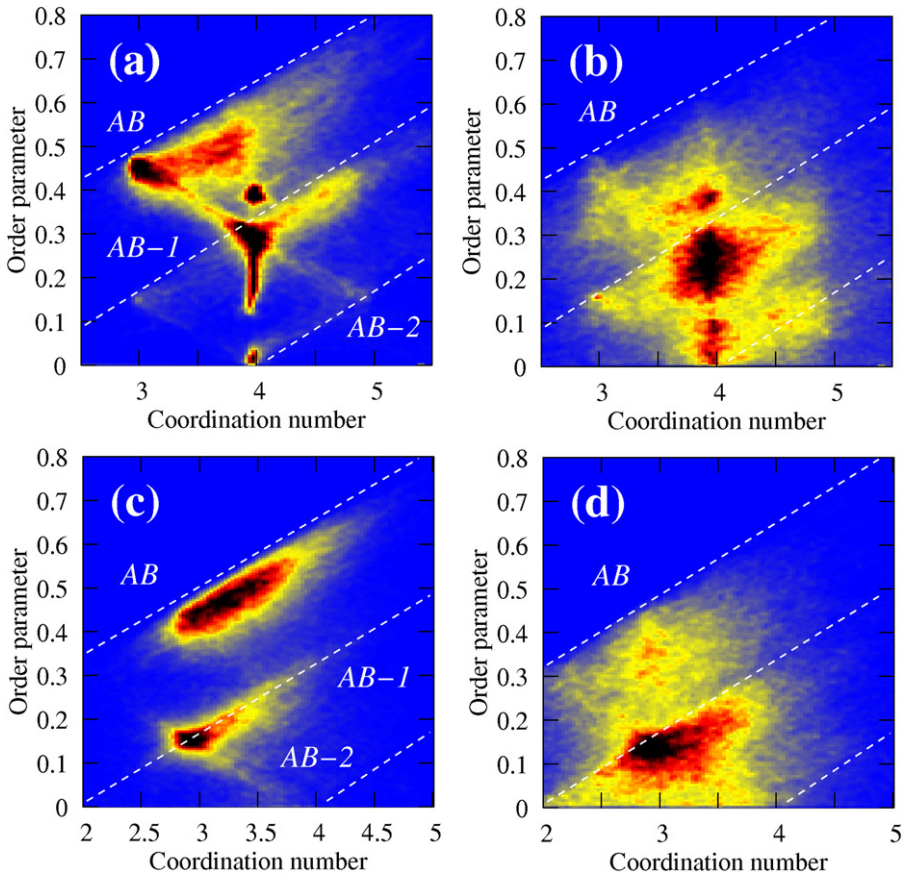

Figure 5. Colour maps of local environment order parameters. Ge atoms at (a) 300 K and (b) 900 K. (c, d) The same for Sb. The diagonal dashed lines mark ideal octahedral bond angles for different degrees of AB ordering (AB, AB–1, AB–2).

parameter with a form similar to (1). The contribution of atom i belonging to type A is written:

$$\alpha_i^{(\mathrm{A})} = \frac{1}{n_\mathrm{B}} \sum_{j \neq i} f(r_{ij}) \frac{\sum_{k \neq i,j} |f(r_{ik})| g(\theta_{ijk})}{\sum_{k \neq i,j} |f(r_{ik})|}, \qquad (2)$$

where n_B is the number of nearest neighbours in the rock salt structure (6, type B). A similar formula holds for contributions from type B (Te) atoms. The sign of $f(r_{ij})$, the cut-off distance for counting nearest neighbours, depends on bond type:

$$f(r_{ij}) = \frac{\pm 1}{\exp[\kappa^{-1}(r_{ij} - r_0)] - 1} \qquad (3)$$

and $g(\theta_{ijk})$ is the angular weighting function:

$$g(\theta_{ijk}) = \cos^2[2(\theta_{ijk} - \theta_0)]. \qquad (4)$$

A–A and B–B bonds ('wrong bonds') give negative contributions, and type A atoms with octahedral coordination to A atoms contribute −1. The order parameter is unity for the rock salt structure with AB alternation and vanishes for a completely disordered system. The parameters ($r_0 = 3.2$ Å, $\kappa = 0.05$ Å, $\theta_0 = 90°$) provide a smooth bond cut-off and reduce the order parameter when the bond angle θ_{ijk} deviates from the angles favoured in the rock salt structure (90° and 180°).

The colour maps of $\alpha_i^{(\mathrm{A})}$ for Ge and Sb (figure 5) combine details of topology (types of neighbours) and structure (bond distances and angles) and are valuable aids to understand the local environment. There are obvious differences between Ge and Sb and between a- and l-GST. At 300 K, Sb atoms (figure 5(c)) prefer octahedral bond angles (dashed lines), whereas the Ge data (figure 5(a)) is more scattered. Furthermore, Ge shows maxima ((4, 0.4) and (4, 0.2)) that correspond to tetrahedral bond angles[5]. Integration over these areas shows that 34% of Ge atoms are tetrahedrally coordinated in a-GST at 300 K. The increased disorder of the liquid is reflected in the variety of configurations (figures 5(b), (d)), but $\alpha_i^{(\mathrm{A})}$ tends to be positive. The weight on threefold coordinated Ge is lower at 900 K, and there are more Ge atoms with higher coordination. Tetrahedral Ge atoms are also prevalent in the liquid (32%). As discussed above, the Sb coordination number is lower in l-GST, as can be seen from the $\alpha_i^{(\mathrm{A})}$ range.

The most common nearest-neighbour configurations of individual atoms in a-GST (300 K) are given in table 3, where we also show for each element the percentage of atoms with a given coordination number. Ge is predominantly fourfold coordinated, and the most common configurations are Ge–Te_4, Ge–Te_3, Ge–$GeTe_3$, and Ge–$SbTe_3$. Sb has a large weight of three- and four-coordinated configurations, the most common

[5] Ge atoms are denoted 'tetrahedral' if the average deviation of the six bond angles from the octahedral values (90°, 180°) exceeds 10°.

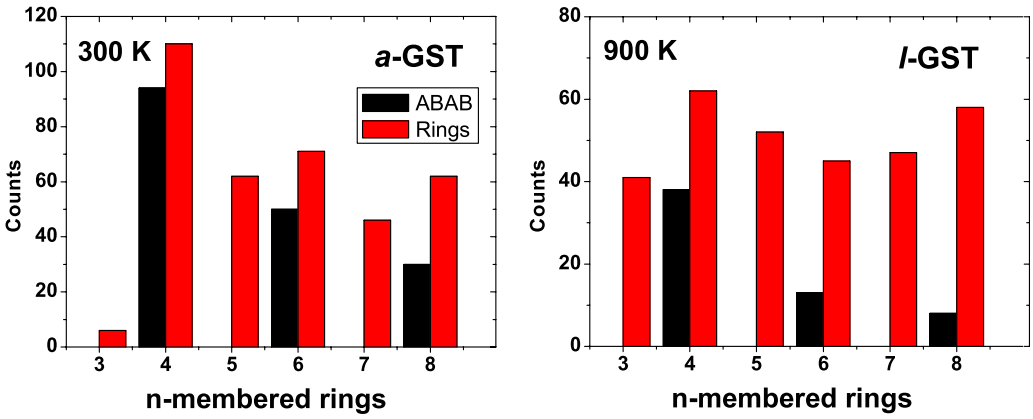

Figure 6. Ring statistics for a-GST (300 K) and l-GST (900 K). ABAB refers to even-membered rings with bond alternation.

Table 3. Nearest-neighbour analysis of a-GST (300 K). The percentage of the total number of atoms of each element are given for configurations with a weight greater than 5%.

	1	2	3	4	5	6
Ge:	<1	<1	21 Te_3: 19.0	53 Te_4: 25.3 $GeTe_3$: 13.4 $SbTe_3$: 10.9	22 Te_5: 7.8 $GeTe_4$: 7.4	4
Sb:	<1	3	48 Te_3: 21.9 $SbTe_2$: 13.9 Sb_2Te: 5.4	37 Te_4: 18.1 $SbTe_3$: 6.8	11 Te_5: 5.7	1
Te:	1	29 Sb_2: 6.2 GeSb: 11.0 Ge_2: 5.9	57 $GeSb_2$: 14.4 Ge_2Sb: 19.9 Ge_3: 6.9	12	1	<1

Table 4. Nearest-neighbour analysis of l-GST (900 K). The percentage of atoms of an element are given for each configuration. We include configurations in table 3 (a-GST, 300 K) or those with a weight greater than 5%.

	1	2	3	4	5	6
Ge:	<1	2	19 Te_3: 10.0	46 Te_4: 12.4 $GeTe_3$: 10.1 $SbTe_3$: 9.6 $GeSbTe_2$: 6.0	27 Te_5: 3.9 $GeTe_4$: 5.1	6
Sb:	2	15 Te_2: 7.3	42 Te_3: 12.9 $SbTe_2$: 9.9 Sb_2Te: 2.8 $GeTe_2$: 7.8 GeSbTe: 5.0	31 Te_4: 6.3 $SbTe_3$: 5.4 $GeTe_3$: 5.5 $GeSbTe_2$: 5.1	9 Te5: 1.0	1
Te:	6	33 Sb_2: 4.1 GeSb: 9.7 Ge_2: 6.0 GeTe: 6.0 SbTe: 5.8	43 $GeSb_2$: 5.6 Ge2Sb: 8.2 Ge_3: 4.0 Ge_2Te: 5.3 GeSbTe: 8.2	16	2	<1

being Sb–Te_3, Sb–Te_4, and Sb–$SbTe_2$. Threefold coordination dominates in Te, with Te–Ge_2Sb, Te–$GeSb_2$, and Te–GeSb occurring most frequently.

We now discuss the colour maps (figures 5(a) and (c)) in more detail. The fourfold coordinated Ge units show a variety of angular configurations, whereas Ge–Te_3, Sb–Te_3, and especially Sb–$SbTe_2$ favour 90° (and 180°). The configurations with fractional number of covalent bonds tend to follow the dashed diagonal lines, so that the local environment of a-GST can be described as 'distorted octahedral' [9] or 'Peierls distorted' [17]. However, numerous Ge atoms are tetrahedrally (sp^3) bonded, where 21% corresponds to Ge–Te_4 units and 13% to Ge–$GeTe_3$ or Ge–$SbTe_3$ units.

GST exhibits interesting differences in the RDF, angular distribution functions, and coordination numbers as a function of T, and table 4 provides additional information. At 900 K, the number of four-coordinated Ge atoms is reduced, but the weight of coordinations 5 and 6 increases by 5% and 2%, respectively. This is consistent with the increase in the total coordination number (table 1). There is less order at 900 K, and the most common configurations are Ge–Te_4, Ge–Te_3, Ge–$GeTe_3$, and Ge–$SbTe_3$. On the other hand, Sb shows a shift to lower coordination (table 1 and figure 5(d)). The increase in the number of twofold coordinated atoms by 12% is compensated by the reduction of three- and four-coordinated Sb. Sb–Te_3 and Sb–$SbTe_2$ remain prominent. The number of threefold coordinated Te is reduced in l-GST, in favour of higher and lower coordinations. Other structural motifs include Te–GeSb, Te–Ge_2Sb, and Te–GeSbTe.

3.4. Ring statistics

We have calculated all irreducible loops (rings) in a- and l-GST using a bond cut-off distance of 3.2 Å and periodic boundary conditions (figure 6), and we focused in [8] on the contribution of alternating ABAB configurations for even-membered rings in a-GST. Fourfold rings dominate the ring statistics at 300 K, and the contribution of ABAB rings (squares) is 86% of the total weight. 52% of atoms participate in at least one ABAB configuration, and this increases to 76% if the bond cut-off is increased to 3.4 Å. Ge occurs 50% more often than Sb, the other type A atom, in the ABAB rings. There are few triangular paths, and odd-membered rings contribute less than even-membered rings (odd–even alternation) [5]. The ring

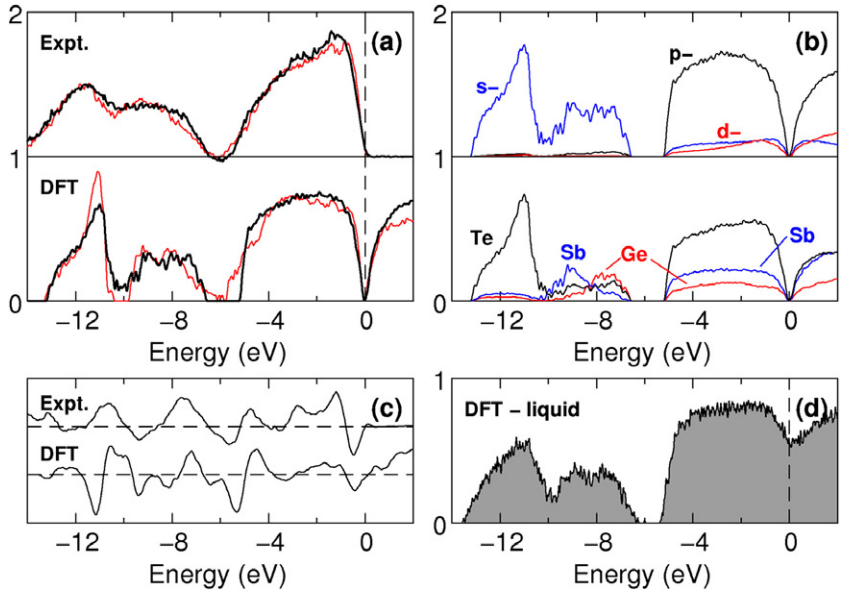

Figure 7. (a) X-ray photoemission spectroscopy (XPS) valence band spectrum of a-(thick black) and c-GST (red/grey lines) ([19], upper panel) and the corresponding theoretical electronic DOS (lower panel). (b) Theoretical DOS of a-GST projected onto atom-centred s-, p-, and d-components and atomic types. (c) DOS difference between c-GST and a-GST (from panel (a)) where positive values indicate a larger weight on a-GST. (d) Electronic DOS of l-GST. The vertical dashed lines mark the Fermi energy.

statistics in l-GST are quite different: The contribution of triangular configurations is much larger, there is no odd–even alternation, and there are fewer ABAB squares.

3.5. Cavities

Crystalline GST contains 10% vacancies, and the density of a-GST is 7% lower. It must contain empty regions (cavities or 'voids', see figure 1(b)), which have been analysed as described in [8]. The volumes have been assigned by applying a construction similar to the Voronoi polyhedron in amorphous materials. For a test particle of radius 2.8 Å, the cavities comprise 11.8% of the total volume of a-GST (slightly more than in the crystal) and 13.8% at 900 K. The cavities are mainly surrounded by Te ($N_{\mathrm{Te}} = 3.8$–3.9), and Sb occurs 50% more often than Ge at 300 K. Both the cavity volume distribution and shapes vary widely.

These cavities (analogous to vacancies in crystalline phases) can accommodate charge. For the 39 cavities in the optimized a-GST sample (figure 1(b)), the integrated charge ranges between 1 and 5 electrons, with an average value of 2.24 electrons. The charge is distributed along the cavity perimeters, and there is no localization at the centre. The definition of a cavity naturally influences the integrated charge found [8].

3.6. Electronic structure and density of states

The electronic density of states (DOS) and its projections are shown in figure 7. The DOS curves have a three-peak structure characteristic of materials with average valence near five. The two lowest bands can be assigned to s electrons (σ band), while the broad band between -5 eV and the Fermi energy has p-character (π band). The band gaps of c- and a-GST are $\sim$0.2 eV at the Fermi energy. These are less than the optical band gaps measured in the amorphous, fcc, and hexagonal phases of GST (0.7 eV, 0.5 eV, 0.5 eV, respectively) [18], and this situation is familiar in calculations using standard DF methods (LDA/GGA). Although the band gaps of the two phases are similar, there is less weight on a-GST DOS at the Fermi energy.

The most visible difference between the DOS in a- and c-GST is the location of the intermediate ('antibonding') σ-band (-10 to -6 eV): In a-GST this band is well separated from the higher lying π-band and merged with the lowest σ-band (-13 to -10 eV), whereas c-GST has a gap at -10 eV. The projected DOS (figure 7(b)) is consistent with the classification into σ- and π-bands; the s-component dominates at lower energies, the p-component closer to the Fermi energy, and the d-component becomes important at higher energies (π-band), where its total weight is similar to that of the s-component. The enhanced d-character can be assigned to Sb atoms.

The atomic projections of DOS show that the lowest σ-band corresponds to Te s-orbitals, and the intermediate band involves all three elements. Furthermore, the π-band is dominated by the Te p-orbitals, and Sb has significantly more weight than Ge. Despite its lower concentration, Sb contributes as much as Te to the conduction band (π-band) in both c-GST and a-GST. The atom-centred projections of the valence band (VB) and conduction band (CB) edges show a noticeable change for c-GST at the Fermi energy (Te-p $\longrightarrow$ Sb-p). The Ge-s contribution for both edges is larger in a-GST than in the crystalline structure, while the Sb-p component of the conduction band is reduced. The wavefunctions of both VB and CB edges have antibonding character.

Photoemission measurements have shown significant differences in the valence band density of states and core levels of a- and c-GST [19, 20] and other Ge/Sb/Te alloys [19].

Table 5. Effective charges of elements (in electrons). The values correspond to charge distribution maxima, and the average values are in parentheses. The modified Voronoi method (last column) includes the charge in cavities.

Method	Mulliken	Voronoi	Voronoi mod.
a-GST			
Ge:	−0.09 (−0.10)	−0.24 (−0.22)	−0.22 (−0.15)
Sb:	0.28 (0.26)	0.30 (0.20)	0.32 (0.34)
Te:	−0.04 (−0.05)	−0.04 (0.09)	0.22 (0.25)
c-GST			
Ge:	−0.10 (−0.12)	−0.25 (−0.25)	−0.22 (−0.24)
Sb:	0.27 (0.29)	0.20 (0.18)	0.22 (0.23)
Te:	−0.04 (−0.06)	0.03 (0.03)	0.20 (0.28)

The differences measured by hard x-ray photoemission spectroscopy (XPS) [19] are compared with our results in figure 7. The agreement is remarkably good, particularly for the DOS difference (figure 7(c)). Furthermore, Kim *et al* [19] report that only the Sb 4d core-level spectrum shows a chemical shift toward lower binding energy. This is consistent with the vanishing band gap at −10 eV as the s–s interaction between Te and Sb increases (i.e., increased Sb 5s contribution at higher binding energies).

The electronic DOS of liquid GST at 900 K (figure 7(b)) and the corresponding projections are similar to a-GST, although the higher temperature leads to broader bands. The gap between the intermediate σ-band and the valence π-band at −6 eV indicates a small s–p mixing. The main difference from the other phases is that the increased disorder results in a finite weight at the Fermi energy, and l-GST is metallic. The projected weights indicate a gradual transition from VB to CB, and the Sb projected component, for example, does not increase abruptly at the Fermi energy as in a-GST. The bands are prominently of p-type, and the CB contribution of Ge and Sb increases gradually while Te remains nearly constant.

There is no unique prescription for calculating atomic charges in covalently bonded materials, and we have calculated Mulliken and Voronoi charges (with or without cavities, see table 5) for a- and c-GST. Both schemes indicate a negatively charged Ge and a positively charged Sb in a-GST. There are clear similarities between a-GST and c-GST, and Sb^+ ions are consistent with the recent work of Kim *et al* [19]. The distribution of Te atoms is broad (Voronoi), with both positive and negative values. Inclusion of cavities in the Voronoi analysis shifts Te charges towards positive values, showing that the charge previously assigned to cavities lies mainly near Te atoms and their lone pair orbitals (p^3 bonding). The Voronoi charges of Te in c-GST underline the similarities between the two phases and the common features of the electronic structure around vacancies/cavities (modified Voronoi).

3.7. Vibration frequencies

The vibration frequencies provide an important means of determining the structures of condensed matter and molecules. In the present work, the frequency distribution (power spectrum) have been calculated in two ways: (a) from the

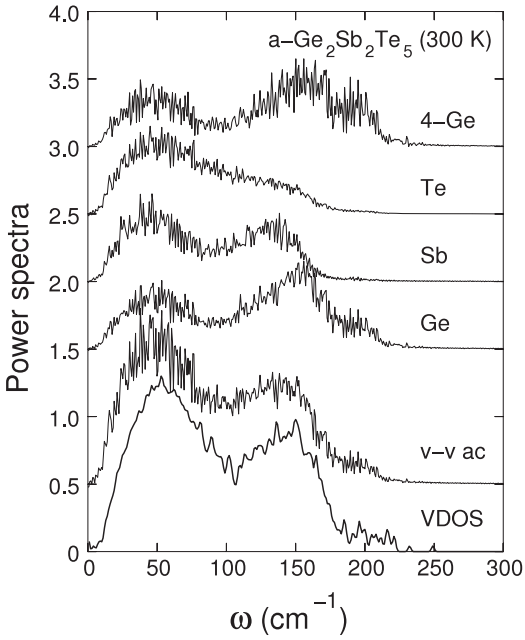

Figure 8. Calculated vibrational density of states for a well-equilibrated sample of a-GST (VDOS, lowest curve), and power spectra from simulation trajectories for a-GST, for Ge, Sb and Te, and for fourfold coordinated Ge atoms ('4-Ge'). The curves have their maximum values at 1.3 (a-GST) or 0.65 (projections).

Fourier transform of the velocity–velocity autocorrelation function C_v:

$$C_v(t) = \frac{1}{N}\sum_{i=1}^{N}\frac{\langle v_i(0)\cdot v_i(t)\rangle}{\langle v_i(0)\cdot v_i(0)\rangle}, \qquad (5)$$

where N is the number of particles, and (b) from the second-order energy derivatives in a well-equilibrated structure. The results of both methods are shown for a-GST in figure 8. The C_v were determined from a trajectory of 6000 time steps of 3.025 fs each, and each vibration frequency in the VDOS was broadened with a Gaussian of width 1 cm^{-1}. The agreement between the vibration frequencies calculated using the two methods is remarkably good. The most pronounced features are peaks ∼60 and ∼150 cm^{-1} and a tail at frequencies above 180 cm^{-1}. Projections onto the vibrations of atoms of different elements (and structural units) show that the tail is associated with vibrations of the lightest element Ge, particularly tetrahedrally bonded Ge atoms (figure 8). Longer simulations would lead, of course, to less noisy spectra.

The power spectrum of c-GST (figure 9) has a narrower frequency range and less pronounced tail than in a-GST. There are broad peaks near 50, 70 and 110 cm^{-1}, and a shoulder near 150 cm^{-1} coming from vibrations of Ge and Sb atoms. The measured Raman spectra (broad peaks at ∼110 and ∼160 cm^{-1} and peaks near 45, 53, and 78 cm^{-1}) differ from those of a-GST films [21], which depend significantly on sample preparation and the temperature of the measurement. For example, in an as-deposited sample a broad peak at 147 cm^{-1} split into peaks at 131 and 152 cm^{-1} on annealing to 200 °C [22]. The Raman spectrum of 100 nm thin films

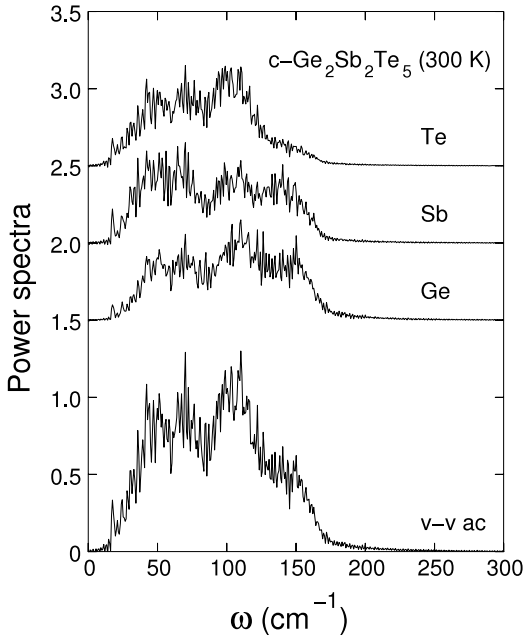

Figure 9. Vibrational density of states calculated for c-GST (lowest curve) and power spectra for vibrations of Ge, Sb, and Te atoms. The curves are scaled to have their maxima at 1.3 (c-GST) or 0.65 (for projected values).

of a-GST [23] has peaks at ∼150 and ∼30 cm^{-1}, which were interpreted as arising from a mixture of stoichiometric (Sb_2Te_3) and non-stoichiometric (GeTe) components.

The sensitivity of vibration frequencies to temperature changes is a promising method for studying phase changes. Reflectivity changes brought about by femtosecond laser pulses have been measured for a-GST and GeTe, c-Sb_2Te_3 and c-GST [24]. Vibrational modes (123 and 160 cm^{-1}) at lower T are replaced between 130 and 150 °C by a mode at 117 cm^{-1} and weaker modes at 67 and 170 cm^{-1}, and this was attributed to the structural transition from amorphous to crystalline (cubic). Another change in the phonon spectrum above 210 °C, with a dominant mode at 50 cm^{-1} and weaker modes at 100 and 170 cm^{-1}, was assigned to the cubic-hexagonal transition. Similar arguments led to the assignment of the cubic structure to rhombohedral Sb_2Te_3 and crystalline β-GeTe. Two frequencies found in a-GST and a-GeTe between room temperature and 130 °C (123 and 160 cm^{-1}) were attributed to the symmetric motions of $GeTe_4$ tetrahedra and disordered Te chains, respectively.

4. Discussion and concluding remarks

We have performed long (several hundred ps) MD/DF simulations of large (460 atoms and 52 vacancies in the unit cell) samples of the amorphous, liquid and crystalline phases of $Ge_2Sb_2Te_5$ (GST) and analysed the structures in terms of RDF, bond angles, and new local order parameters. Charges in the atoms and vacancies (cavities) have been calculated using the Mulliken and Voronoi methods. Vibration frequencies in a-GST determined from the diagonalization of the dynamical matrix and from the Fourier transform of the velocity–velocity

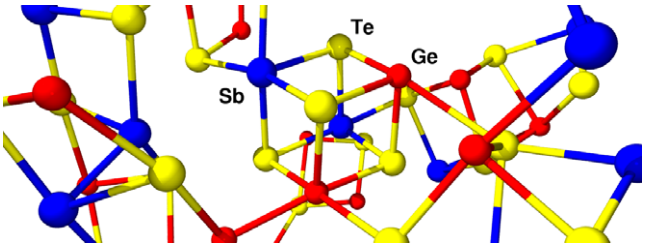

Figure 10. A cubic ABAB subunit in a-GST. A Ge–Ge bond (between the cube and its neighbours) and an Sb–Sb bond are evident. Cavities occur near the cube, and a threefold coordination is typical for Te.

autocorrelation function agree extremely well. Projected vibrational densities of states provide additional information.

The structures of a- and c-GST show numerous similarities: (i) AB alternation, (ii) octahedral bond angles, and (iii) vacancies (cavities), which play an essential role in the phase change. These similarities, which we proposed [8] as a reason for the rapid a–c phase transition, are reflected in the calculated electronic DOS, which are strikingly similar to the experimental valence XPS spectra [19], and in the atomic charges. Sb is positively charged in both cases. Vacancies (cavities) contain charge originating in neighbouring Te atoms, and the over-coordination of Sb in a-GST is related to this charge transfer. The fourfold ABAB rings (squares) common in a-GST occur in c-GST as ordered ABAB squares. Cubic subunits occur in a-GST (see figure 10) and there are other configurations where slight changes in the structure would result in a 'cube'. ABAB squares are consistent with the tendency to form octahedral bonds.

The structures of the disordered phases are much more complicated than those assumed in analysing earlier experiments on a-GST, e.g. Ge–Te_4 tetrahedra or Te_3-Ge–Ge–Te_3 units [13, 14]. Fourfold Ge–Te_4 species are the most abundant single configuration in our simulations, but their weight (25.3%) is not large, and the small number of Ge–Te_3 configurations (13.4%) indicates that dimeric units (Ge_2Te_3) are unlikely [14]. 53% of Ge atoms are fourfold coordinated, and roughly one-third have tetrahedral bond angles (see footnote 4). Other MD/DF simulations of a-GST [9] also point to the coexistence of tetrahedral- and octahedral-like sites. These points indicate that the 'umbrella flip' of tetrahedral Ge atoms to octahedral sites [13] is unlikely to explain the rapid a–c transition in GST. We also note that DF calculations [7] predict that there is no energy barrier between these structures, so the tetrahedral structure proposed in reference [13] would relax to the crystalline form.

The coordination numbers (Ge: 4.2 (4.3); Sb: 3.7 (3.4); Te: 2.9 (2.8) at 300 K (900 K)) differ from those (4, 3, 2) that would result from the '8–N rule', where N is the valence of the element. The coordination of Te (∼3) and its effect on those of Ge and Sb are in marked contrast to the RMC analysis of data from x-ray diffraction, neutron diffraction, and Ge, Sb, and Te K-edge EXAFS measurements [15], where all atoms satisfy the above rule. If Te is twofold coordinated, the '$8 - N$ rule' requires homopolar ('wrong') bonds in a-GST to compensate the higher coordination numbers forced on Ge and Sb. Such

bonds do occur in the present work, but they contribute little. The number of Ge–Sb bonds is lowered on cooling from the liquid (the coordination number changes from 0.6 to 0.2), and this is also true for Te–Te bonds (reduction from 0.7 to 0.3). The small number of 'wrong bonds' is consistent with the pronounced AB alternation in a-GST.

Acknowledgments

The calculations were performed on IBM Blue Gene/L, Blue Gene/P and p690 computers in the Forschungszentrum Jülich with grants from the FZ Jülich and the John von Neumann Institute for Computing (NIC). We thank S Kohara and K Kobayashi for helpful discussions and original data.

References

[1] Yamada N, Ohno E, Akahira N, Nishiuchi K, Nagat K and Takao M 1987 *Japan. J. Appl. Phys.* **26** (Suppl. 26-4) 61
[2] Yamada N 1996 *Mater. Res. Soc. Bull.* **21** 48
[3] Yamada N and Matsunaga T 2000 *J. Appl. Phys.* **88** 7020
[4] Nonaka T, Ohbayashi G, Toriumi Y, Mori Y and Hashimoto H 2000 *Thin Solid Films* **370** 258
[5] Kohara S *et al* 2006 *Appl. Phys. Lett.* **89** 201910
[6] See for example, Ballone P and Jones R O 2001 *J. Chem. Phys.* **115** 3895
Kohary K, Burlakov V M and Pettifor D G 2005 *Phys. Rev.* B **71** 235309
[7] Lang C, Song S A, Manh D N and Cockayne D J H 2007 *Phys. Rev.* B **76** 054101
[8] Akola J and Jones R O 2007 *Phys. Rev.* B **76** 235201
[9] Caravati S, Bernasconi M, Kühne T D, Krack M and Parrinello M 2007 *Appl. Phys. Lett.* **91** 171906
[10] Hegedüs J and Elliott S R 2008 *Nat. Mater.* **7** 399
[11] CPMD V3.11 Copyright IBM Corp 1990–2006 *Copyright MPIfür Festkörperforschung Stuttgart 1997–2001* (http://www.cpmd.org)
[12] Sato M, Matsunaga T, Kouzaki T and Yamada N 2004 *Mater. Res. Soc. Symp. Proc.* **803** 245
[13] Kolobov A V, Fons P, Frenkel A I, Ankudinov A L, Tominaga J and Uruga T 2004 *Nat. Mater.* **3** 703
[14] Baker D A, Paesler M A, Lucovsky G, Agarwal S C and Taylor P C 2006 *Phys. Rev. Lett.* **96** 255501
[15] Jóvári P, Kaban I, Steiner J, Beuneu B, Schöps A and Webb A 2007 *J. Phys.: Condens. Matter* **19** 335212
[16] Ruppersberg H and Wagner C N J 1983 *J. Non-Cryst. Solids* **55** 165
[17] Bichara C, Johnson M and Gaspard J P 2007 *Phys. Rev.* B **75** 060201(R)
[18] Lee B-S, Abelson J R, Bishop S G, Kang D-H, Cheong B and Kim K-B 2005 *J. Appl. Phys.* **97** 093509
[19] Kim J-J, Kobayashi K, Ikenaga E, Kobata M, Ueda S, Matsunaga T, Kifune K, Kojima R and Yamada N 2007 *Phys. Rev.* B **76** 115124
[20] Lee D *et al* 2007 *Appl. Phys. Lett.* **91** 251901
[21] Yoon H R, Jo W, Cho E, Yoon S and Kim M 2006 *J. Non-Cryst. Solids* **352** 3757
[22] Tominaga J and Atoda N 1999 *Japan. J. Appl. Phys.* **38** L322
[23] Andrikopoulos K S, Yannipoulos S N, Kolobov A V, Fons P and Tominaga J 2007 *J. Phys. Chem. Solids* **68** 1074
[24] Först M, Dekorsy T, Trappe C, Laurenzis M, Kurz H and Béchevet B 2000 *Appl. Phys. Lett.* **77** 1964